

# **JGR** Solid Earth

# <del>-</del>

## RESEARCH ARTICLE

10.1029/2024JB030425

## **Key Points:**

- We present a multi-scale 3D velocity model for Krafla volcano obtained by Local Earthquake Tomography (LET) for imaging and seismicity monitoring
- We show the potential of an established imaging method like LET with a very dense station distribution
- We could map zones in the upper crust where fluids are present with different phases and compositions

#### **Supporting Information:**

Supporting Information may be found in the online version of this article.

#### Correspondence to:

E. Glück, elisabeth.gluck@univ-smb.fr

#### Citation:

Glück, E., Garambois, S., Vandemeulebrouck, J., Muzellec, T., Virieux, J., Mortensen, A. K., et al. (2025). Seismicity patterns and multi-scale imaging of Krafla, N–E Iceland, with local earthquake tomography. *Journal of Geophysical Research: Solid Earth*, *130*, e2024JB030425. https://doi.org/10.1029/ 2024JB030425

Received 26 SEP 2024 Accepted 11 MAY 2025

#### **Author Contributions:**

Stéphane Garambois,
Jean Vandemeulebrouck
Methodology: Elisabeth Glück,
Stéphane Garambois,
Jean Vandemeulebrouck,
Titouan Muzellec, Jean Virieux
Resources: Anette K. Mortensen, Egill
Árni Gudnason, Thorbjörg Ágústsdóttir
Software: Titouan Muzellec
Supervision: Stéphane Garambois,
Jean Vandemeulebrouck
Visualization: Elisabeth Glück
Writing – original draft: Elisabeth Glück

Conceptualization: Elisabeth Glück,

© 2025. The Author(s).

This is an open access article under the terms of the Creative Commons

Attribution-NonCommercial-NoDerivs

License, which permits use and distribution in any medium, provided the original work is properly cited, the use is

non-commercial and no modifications or

Seismicity Patterns and Multi-Scale Imaging of Krafla, N–E Iceland, With Local Earthquake Tomography

Elisabeth Glück<sup>1</sup>, Stéphane Garambois<sup>1</sup>, Jean Vandemeulebrouck<sup>1</sup>, Titouan Muzellec<sup>2</sup>, Jean Virieux<sup>1</sup>, Anette K. Mortensen<sup>3</sup>, Egill Árni Gudnason<sup>4</sup>, and Thorbjörg Ágústsdóttir<sup>4</sup>

<sup>1</sup>University Grenoble Alpes, University Savoie Mont Blanc, CNRS, IRD, Univ. Gustave Eiffel, ISTerre, Grenoble, France, <sup>2</sup>Universita degli Studi di Napoli Federico II, Naples, Italy, <sup>3</sup>Landsvirkjun, Reykjavík, Iceland, <sup>4</sup>ÍSOR, Iceland GeoSurvey, Kópavogur, Iceland

Abstract Krafla, one of five central volcanoes of the Northern Volcanic Zone in Iceland, is utilized for geothermal energy production. Due to scientific and industrial interests, the volcano and its geothermal system have been imaged and monitored with various geophysical methods over the last decades leading to a better knowledge of its complex geological setting. Nonetheless, the unexpected encounter of magma at relatively shallow depths during drilling of the IDDP-1 well in 2009 proved that imaging small-scale structures remains challenging in such heterogeneous geological settings. With data from a local permanent 12 station seismic network owned by Landsvirkjun and operated by Iceland GeoSurvey since 2013, and a dense temporary network of 98 seismic nodes deployed for one month in 2022 in the center of Krafla caldera, we conducted a multi-scale analysis based on local earthquake tomography. This analysis enables us to identify small-scale velocity structures and improve earthquake locations. The newly obtained high-resolution 3D models for P- and S-wave velocities offer a glimpse into the subsurface structure of the volcanic system with both wave types being responsive to distinct rock/fluid properties. The relocated seismic activity highlights active structures pinpointed through the tomography, in particular the seismogenic zone at the boundary of high to low  $V_n/V_s$ ratios, close to where magma was repeatedly encountered. By comparing the newly obtained high-resolution velocity models with available well log data, such as formation temperature, we aim to enhance the understanding of the interconnected volcanic and geothermal systems in areas lacking in situ measurements.

**Plain Language Summary** Krafla is one of five volcanic systems of the Northern Volcanic Zone in northeast Iceland and its geothermal system has been utilized for decades for geothermal energy production. Even though Krafla has been thoroughly monitored and imaged, in 2009, the IDDP-1 well, which was intended to reach super-critical fluids at 4–5 km depth, was drilled into magma at only 2.1 km depth. This unexpected encounter reveals that the previous large-scale model obtained from geophysical imaging was unable to identify crucial small structures such as magma batches. In this study, we combined data from a large-scale permanent and a dense small-scale temporary seismic network to conduct a multi-scale experiment, leveraging the strengths of both setups. By analyzing the recorded earthquakes from both networks, we reconstructed both lowand high-resolution velocity models. The low-resolution model improves seismicity location reliability, while the high-resolution model provides previously unknown detailed insights into the subsurface velocity structure of the volcano.

## 1. Introduction

## 1.1. Volcanic Geothermal Systems—Seismicity and Imaging

High-temperature geothermal systems have been utilized for decades for power production, the oldest ones being Lardarello (Italy) since 1948, Wairakei (New Zealand) since 1958 and the Geysers (USA) since 1965 (Sanyal & Enedy, 2011). This type of geothermal reservoir is only found in volcanic areas (Sæmundsson et al., 2009), which are commonly seismically active, with various internal processes generating different types of seismic events (Wassermann, 2012). The continuous production of geothermal energy with the migration of fluids adds another potential source of seismicity, making the understanding of the recorded seismic activity more complex. For geothermal energy production, steam and/or fluids are extracted and re-injected (Elíasson et al., 2014; Flóvenz et al., 2015), altering the reservoir temperature and pressure, potentially leading to stress changes that might generate seismicity along pre-existing faults (Buijze et al., 2019; Einarsson & Brandsdóttir, 2021; Mossop, 2001;

adaptations are made.



# Journal of Geophysical Research: Solid Earth

10.1029/2024JB030425

Writing – review & editing: Stéphane Garambois, Jean Vandemeulebrouck, Anette K. Mortensen, Egill Árni Gudnason, Thorbjörg Ágústsdóttir Sewell et al., 2015). Regardless of whether the seismicity is natural or anthropogenic, seismic monitoring is important for detecting active structures, geological entities and potentially fluid characteristics.

A reliable location of seismicity, particularly with respect to depth, is challenging with a poorly constrained velocity model (Husen et al., 2003). The nonlinear bias between location and velocity parameters makes Local Earthquake Tomography (LET) difficult for an upper crust analysis (Latorre et al., 2004; Vanorio et al., 2005). However, this method gives new insights into different volcanic and geothermal systems like the Geysers in the US (Lin & Wu, 2018), Lardarello in Italy (Bagagli et al., 2020; Vanorio et al., 2004) and Krafla in Iceland (Schuler et al., 2015). The reconstructed P- and S-wave velocities ( $V_p$  and  $V_s$ ), and the  $V_p/V_s$  ratio in case of the Geysers (Lin & Wu, 2018), together with the related event locations, bring significant information on the local geological structures and the fluid/gas content.

However, in most cases, permanent seismic networks are installed for monitoring seismicity within the respective geothermal system rather than for seismic tomography, and only a limited number of stations is available for long time periods. These network configurations cover the geothermal systems as evenly as possible, but leave the imaging ability of LET less exploited. In this paper, we analyze the contribution of a dense temporary seismic network embedded into the sparser permanent network at Krafla with the aim of improving the velocity reconstruction as well as obtaining reliable locations of the seismicity within a complex volcanic caldera.

## 1.2. The Krafla Volcanic System

Through its unique geological setting, where the Iceland hotspot and the divergent Mid-Atlantic ridge coincide, Iceland has a long history of geothermal utilization. Since around 1930, geothermal energy is used for heating and since 1968 for the generation of electricity (Ragnarsson et al., 2023). Krafla is located in northeast Iceland, within a 90 km long, NNE–SSW trending fissure swarm, which is part of the rifting Northern Volcanic Zone of Iceland (Figure 1). Superimposed on the fissure swarm is a central volcano of about 20 km in diameter. A 8–10 km wide caldera was formed approximately 110 ka ago, which is now elongated in E–W direction due to rifting (Figure 1, black toothed line), and within the caldera structure is a NW–SE elongated and developed high-temperature geothermal area (Sæmundsson, 1991; Sæmundsson et al., 2000). A power plant was built at Krafla in the early 1970s, and both scientific and industrial interest has led to extensive surveying of the volcano and its geothermal system with a wide variety of geophysical methods over the last 50 years. Different large-scale geophysical surveys of active seismic experiments, seismic tomography, gravity and magneto-telluric measurements show a high  $V_p$  anomaly, that is dense and resistive in the area of the caldera boundary. In the center of the caldera, where the presence of a magma chamber at 3 km depth is suggested (Brandsdóttir et al., 1997; Einarsson, 1978), densities and P-wave velocities are lower, and conductive bodies are mapped out (Árnason, 2020; Arnott & Foulger, 1994; Lee et al., 2020; Schuler et al., 2015).

A transverse structure perpendicular to the rifting fissure swarm (Figure 1, T1 and T2) and the possible existence of a second inner caldera (Figure 1, black dashed line) were proposed by Árnason (2020). The transverse structure, delimited by ESE–WNW oriented white lines in Figure 1 (T1 and T2), is identified as a resistive body in the resistivity model and as a low density structure in the gravity model presented by Árnason (2020). In the seismic tomography of Schuler et al. (2015), the parts of this structure that are illuminated by seismic rays exhibit high  $V_{\rm p}/V_{\rm s}$  values in the uppermost kilometers.

Apart from larger caldera forming eruptions, smaller eruptions at Krafla have occurred during the recent Holocene at 300–1,000 years intervals, the last two being the Mývatn Fires from 1724 to 1729 (Sæmundsson, 1991) and the Krafla Fires from 1975 to 1984 (Einarsson, 1991). The geologically complex stratigraphy covers more than the last 300 ka of Kraflas eruptive history during both glacial and interglacial conditions constituting extrusive hyaloclastites and intrusive basalts and rhyolites, partly altered by the hydrothermal system (Ármannsson et al., 1987; Árnason, 2020; Mortensen et al., 2015; Scott et al., 2022). These small-scale structures were mapped along very localized profiles by reflection seismics, micro-seismicity analysis or vertical seismic profiling (Kim et al., 2020; Reiser et al., 2020), highlighting boundaries in the lithology and possibly identifying the top of a shallow magma body.

The combination of a fissure swarm superimposed on a central volcano gives a complex geological framework of layers, fractures and faults, that pose either pathways or barriers to fluids. They can be divided into three main groups: (a) features perpendicular to the minimum horizontal stress of the plate movement (e.g., the NNE–SSW

GLÜCK ET AL. 2 of 20

21699556, 2025. 5, Downboaded from https://agupubs.onlinelibrary.wiley.com/doi/10.1029/20241B030425 by Ingv, Wiley Online Library on [11/11/2025]. See the Terms and Conditions (https://onlinelibrary.wiley.com/rems-and-conditions) on Wiley Online Library for rules of use; OA articles are governed by the applicable Creativity of the applicable Creativity of the applicable of the applicable

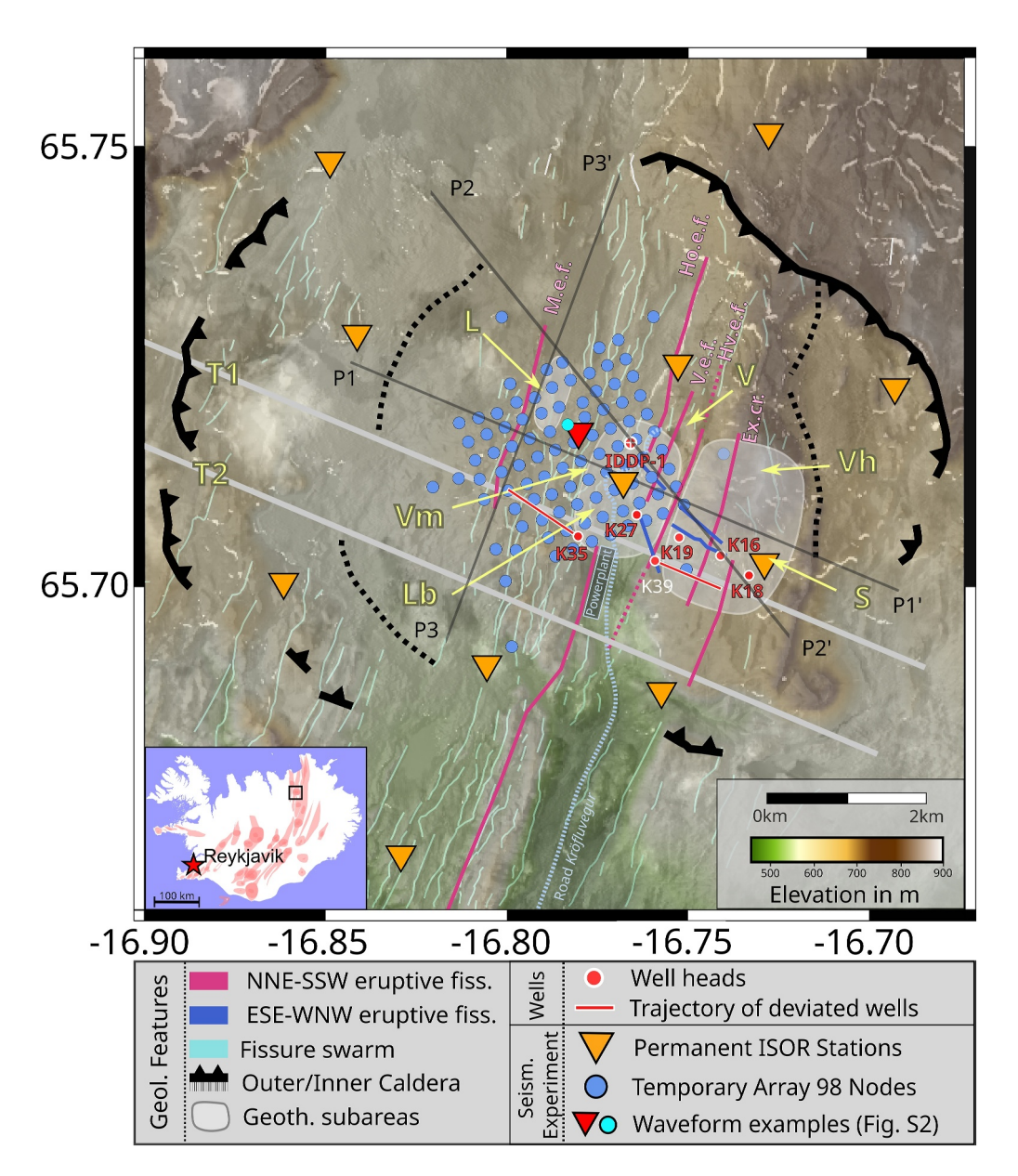


**Figure 1.** Overview of the main structural features of Krafla. Black (solid, toothed) line shows the caldera rim, while pink and blue lines are eruptive fissures mapped in Mortensen et al. (2015). The inner caldera (black dashed line) and the transverse structure (delimited by white lines, T1 and T2) are proposed by Árnason (2020) and are still debated. The large-scale (orange triangles) and small-scale (blue dots) seismic networks at Krafla, with the location of selected wells with available formation temperature, except K-39 (red circles, white edge). The trajectory of deviated wells is shown in red with a white edge. Red triangle: LHN permanent station. Light blue circle: Node 59 whose signals are shown in Supporting Information S1. P1–P3 mark the cross-sections shown in Figures 3 and 7. Abbreviations: L: Leirhnjúkur, Lb: Leirbotnar, S: Suðurhlíðar, V: Víti, Vh: Vesturhlíðar, Vm: Vítismór, M.e.v.: Mývatn fire eruptive fissure, Ho.e.f.: Hóls fire eruptive fissure, V.e.f.: Víti fire eruptive fissure, Hv.e.f.: Hveragil fire eruptive fissure, Ex.Cr.: Row of holocene explosive craters. Inset: Location of Krafla in Iceland (based on Johannesson and Saemundsson (1999); Johannesson and Saemundsson (1998a, 1998b) and modified after Scott et al. (2022)).

trending fissure swarm, eruptive fissures in this direction (pink lines in Figure 1)), (b) features due to shear stress (e.g., the WNW-ESE oriented eruptive fissures in this direction (blue lines in Figure 1) and, though its origin is debated, potentially the structure between T1 and T2 in Figure 1), and (c) fractures and faults associated with the central caldera (Ármannsson et al., 1987; Sæmundsson et al., 1999).

GLÜCK ET AL. 3 of 20

A study of seismic anisotropy based on shear wave splitting (Tang et al., 2008) supports these 3 main groups of features induced by the superimposed stress fields. The high seismic anisotropy may have an effect on the travel times used for the LET (Koulakov et al., 2009), though it is beyond the scope of this work to consider.

## 1.3. The Krafla Geothermal System

The Krafla geothermal system occupies the center of the caldera with estimated reservoir temperatures up to 350 °C at 2 km depth (Ármannsson et al., 1987; Bodvarsson et al., 1984). Over the last decades, up to 40 wells have been drilled, with some extending down to around 2,000 m b.s.l. Most of the wells are used to extract hot fluids and steam, while a few are used for re-injection of cold water (Mortensen et al., 2015).

Well formation temperatures, pressure logs (Ármannsson et al., 1987; Bodvarsson et al., 1984; Mortensen et al., 2015) and a fluid flow model proposed by Scott et al. (2022) suggest the existence of sub-fields with different geothermal properties. In the central production area of Leirbotnar and Vítismór (Figure 1), an isothermal system of 200 °C down to 500–1,000 m b.s.l., is overlying a 2-phase fluid zone, where temperatures follow the boiling point curve with depth. In Suðurhlíðar, the eastern part of the geothermal production field that is separated from the others by the Hveragil fault, the formation temperature is following the boiling point curve from the surface (Árnason, 2020; Mortensen et al., 2015). In the western part of Krafla (Leirhnjúkur), close to the fissure swarm and the lava fields of the two most recent eruptions, there is only one well, K-35, southwest of Leirhnjúkur. The formation temperature of K-35 as well as high surface temperature and  $CO_2$  flux (Bini et al., 2024) suggest the presence of another high-temperature geothermal field in this area.

The 3D body wave tomography of Schuler et al. (2015) identifies a low  $V_p/V_s$  zone, suggesting gas saturation in the center of the caldera, beneath the main production area at 2–3 km depth. A high  $V_p$  anomaly is located 3 km underneath Leirhnjúkur, coinciding with a conductive body (Lee et al., 2020) and S-wave shadows mapped by Einarsson (1978) during the Krafla fires. These geophysical observations align with the fluid-flow model of Scott et al. (2022), suggesting that underneath the boiling zone, sampled by the wells in the central and eastern part of Krafla, a single-vapor zone is overlying a heat source, for example, a magmatic body. In 2009, the Icelandic Deep Drilling Project tried to reach super-critical conditions expected at 4–5 km depth with the IDDP-1 drilling, but instead magma was found at 2.1 km depth (Mortensen et al., 2014, 2015). Also well K-39, drilled a year before in the southeastern part of the geothermal field, encountered magma at 2.6 km depth (Mortensen et al., 2010). The presence of one larger or multiple smaller magma batches at these depths, as well as in situ information from other drillings, offer the opportunity to better constrain geophysical and conceptual models of the volcanic and geothermal system. Even though there is already some knowledge of Kraflas sub-surface, resolving small-scale structures of this system still poses challenges and leaves uncertainties, as shown by the unexpected breakthrough of magma when the two wells, IDDP-1 and K-39, were drilled.

In this work, our aim is to image the different structures with the highest possible resolution, insofar as the LET technique allows, benefiting from the contribution of two seismic networks of different sizes. The imaging of velocity structures aims not only at a global structural interpretation, but also at a more precise location of the seismicity. This can then in turn highlight the active structures and reveal the physical processes within the Krafla volcano and its geothermal system.

## 2. Data and Pre-Processing

Here, two seismic networks are considered for seismic imaging and monitoring purposes: a large-scale permanent seismic network (12 stations) and a small-scale temporary network of 100 nodes, installed for one month (Figure 1). The aim of this multi-scale study is first to compare these two very different data sets in terms of event location performance and structural imaging. In a second step, these data sets are merged to take advantage of the extensive number of events and stations to retrieve high-resolution structural models with a large number of accurate event locations.

## 2.1. The Large-Scale Network

At Krafla, a permanent network of 12 stations with different sensors (bandwidth: 1–200 Hz or 5 s–200 Hz), owned by the Icelandic national power company, Landsvirkjun, and operated by Iceland GeoSurvey (ÍSOR), has been running since 2013 to monitor seismicity. Six of the seismometers are installed in geothermal wells at various

GLÜCK ET AL. 4 of 20

21699356, 2025, 5, Downloaded from https://agupubs.onlinelibrary.wiley.com/doi/10.1029/2024JB030425 by Ingv, Wiley Online Library on [11/11/2025]. See the Terms

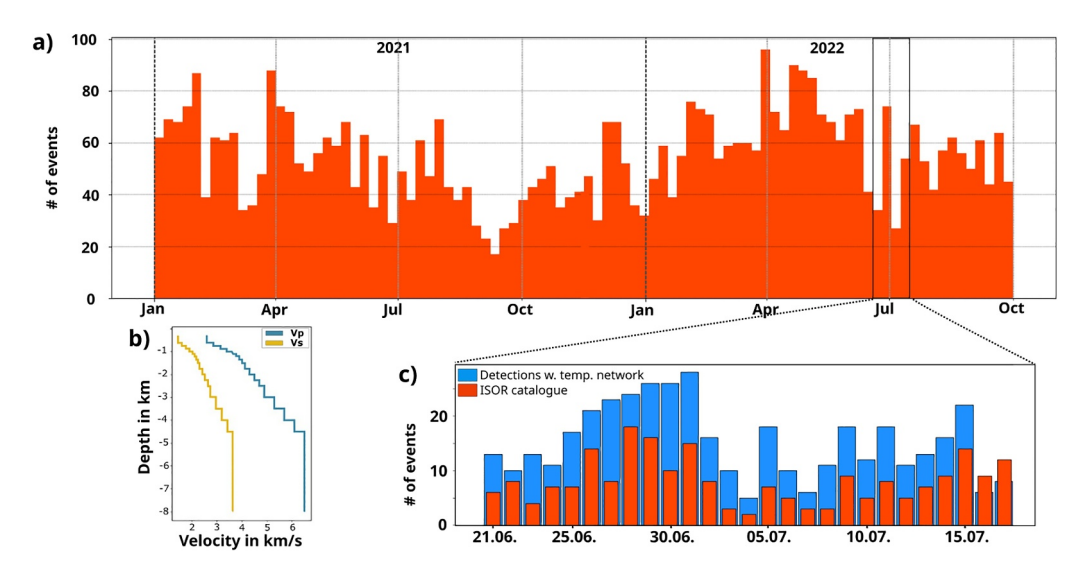


**Figure 2.** Earthquake catalogs: (a) the ÍSOR catalog from 2021 to 2022, (b) the layered 1D velocity model used for the location in the ÍSOR catalog (Guðnason et al. (2023) and references within), and (c) the detections of the temporary small-scale network in June–July 2022 in blue, compared with the events in the ÍSOR catalog in red.

depths, ranging from 9 to 60 m. The waveforms of the seismic events detected at these stations were provided by ÍSOR, along with manual P- and S-picks (see Wadati-diagram of the picks in Text S1 and Figure S1 in Supporting Information S1) for all events in the catalog proposed by Guðnason et al. (2023) (referred to as ÍSOR catalog hereafter). For the imaging, it was decided to only use a subset of events from the ISOR catalog to reduce the computation time of the tomography, since the distribution of the earthquakes is spatially stable over time, providing similar ray paths. The period from January 2021 to September 2022 was chosen, since the occurrence of seismicity was at a comparatively low but constant level (Figure 2a), providing good ray coverage. In addition, deformation data (GNSS) shows that Krafla was neither in- nor deflating during that time, therefore no drastic changes of the underground velocities are expected. Also, the temporary stations of the small-scale network were installed during this period, keeping the results of both networks comparable.

Within this period, the ÍSOR catalog contains manually refined picks of  $\sim$ 32,300 P- and  $\sim$ 25,200 S-wave onsets from  $\sim$ 3,700 events. Those events were located with a layered 1D velocity model (Guðnason et al. (2023) and references within). The picks, event locations, and the velocity model are both used as input for the LET (Figure 2b).

## 2.2. The Small-Scale Network

In June and July 2022, a network of 100 3-component Fairfield seismic nodes (short period > 5 Hz) was deployed with a 250 m spacing in the center of the caldera, 98 of them recording from June 21 (first full day) and lasting for 25–30 days. The ÍSOR catalog contains 193 events between June 21 and July 17, the day on which a majority of the nodes started failing due to weak batteries. For these 193 events, P- and S-wave onsets were picked manually on the 98 nodes to be able to compare the results of the event location and tomography for both networks on the same set of events. However, with the dense station distribution, 465 events could be detected in total (Figure 2c) by using template matching and STA/LTA algorithms (Text S2 and Figure S2 in Supporting Information S1).

## 2.3. Manual Picks and Assigned Picking Errors

Picking errors for the manually picked P- and S-wave onsets are needed as an additional input in every step of the following workflow of event location and tomography, to assign a weight to each pick. To quantify the picking errors (±a certain time range) for the picks at each stations of both networks, a signal-to-noise ratio (SNR) was calculated for each P- and S-pick from broadband filtered seismograms, based on the amplitude ratio before and after the pick.

GLÜCK ET AL. 5 of 20

21699356, 2025, 5, Downloaded from https://agupubs.onlinelibrary.wiley.com/doi/10.1029/2024JB030425 by Ingv, Wiley Online Library on [11/11/2025]. See the Terms and Conditions

Given thresholds for the calculated SNR are used to assign the picking errors, that are different for P- and S-wave onsets. For the S-waves, the SNR was calculated on both horizontal components, and the higher SNR value was used to assign the picking error (example of the waveforms and the picking in Text S3 and Figure S3 in Supporting Information S1). Reasons for a high picking error may be an overall low SNR or an emergent onset of the arriving wave. If the SNR is below a certain threshold, the pick is discarded.

#### 3. Methods

## 3.1. Local Earthquake Tomography

To perform a LET, initial velocity models and initial earthquake locations are needed. The LET workflow is a linearized inversion process updating velocity model parameters and earthquake parameters (Kissling et al., 1994; Thurber, 1992). For the location of the source origin in time and space (Text S4 in Supporting Information S1), not only the observed arrival time at the receiver is needed, but also a velocity model. Both, the origin and the observed times are linked through rays traveling on a path from the source through the medium to the station by the Eikonal equation (Lomax et al., 2009), which makes the relation non-linear. However, the velocities can only roughly be estimated, thus leading to a difference in calculated and observed arrival times, called residuals. To minimize those differences, the LET fits the location and time of an earthquake in small steps with an iteratively updated velocity model, where small perturbations of the velocity model and the origin are used to find the minimum value of the misfit function for all stations, which are then added to the current values for the next iteration.

The code TomoTV (Latorre et al., 2004), which is based on ray theory, is used to retrieve 3D P- and S-wave velocity models and improved earthquake locations, with the previously obtained locations and an initial velocity model as input. With a nodal approach, a rectangular grid is specified with regular discretization and a linear interpolation is assumed inside each cell.

#### 3.1.1. Discretization of the Forward and Inversion Grids

Discretizing the rays and the velocity model with a fine forward and a coarser inverse gridding, linearizes iteratively the non-linear inversion problem (Latorre et al., 2004; Vanorio et al., 2005; Virieux et al., 2024). The discretized rays are obtained by solving the Eikonal equation for each receiver and by backtracing. For this forward modeling, the ray is traced through a finely discretized subsurface on its way from the source to the station. Theoretical travel times are then computed and the partial derivatives of the velocity nodes and hypocenter parameters are estimated. The inversion grid cell size, on the other hand, should be chosen larger than the forward gridding, but smaller than the expected spatial resolution (Virieux et al., 2024). The theoretical maximum resolution, according to the first Fresnel zone is approximately  $\sqrt{\lambda} L$  where  $\lambda$  is the wavelength and L the distance of source and receiver, or roughly the depth of the seismicity regardless of the station distribution. Assuming that the first P-wave onset has a frequency of 5–10 Hz and the mean P-wave velocity is around 3,500 m/s for events at 1.8 km depth, a fraction of a kilometer can be estimated as resolution, which is expected from first-arrival interaction between wave and medium. However, smaller structures may have possible imprints within the reconstructed velocity models, mainly related to the station density of the seismic network benefiting from different Fresnel zones, though such high-resolution velocity variations should be handled with care (Li & Duric, 2013).

# 3.1.2. Setting of the Hyperparameters

Next to the input parameters of arrival time picks, picking errors and the iteratively adjusted input of velocity model and event locations, hyperparameters have to be defined to balance the joint inversion. To find the best trade-off between data and model fit, the L-curve (Hansen, 1999) was used for selecting the damping and smoothing parameters. While the damping is a way of driving the inversion by adjusting the velocities and locations in larger or smaller steps, the setting of the smoothing parameters avoids or allows sharp velocity contrasts when fitting the model to the data. The other hyperparameters like the weighting between source origin parameter and velocity model were set by a penalty approach, where it was observed that weighting the source origin higher than the velocity parameters led to a faster convergence with a lower RMS. The origin of the inversion grid,

GLÜCK ET AL. 6 of 20

21699356, 2025, 5, Downloaded from https://agupubs.

.com/doi/10.1029/2024JB030425 by Ingv, Wiley Online Library on [11/11/2025]. See the Terms

use; OA

usually chosen randomly, was also shifted several times to check if edge effects were generated by this random selection of the grid origin, which was not the case.

## 3.2. From Differently Scaled Networks to Multi-Scale Imaging

Velocity structures can only be retrieved in areas where rays pass through the inversion grid cells, and since the events and receivers for this multi-scale experiment are not evenly distributed, there are areas that can be better resolved than others.

If only the large-scale permanent network is used, the distribution of the ray density is very heterogeneous with some parts of Krafla being very well illuminated by a high number of repeating rays, while others are not sampled at all. When the small-scale temporary stations are added, the upper central part of the Krafla caldera is illuminated, though there are still gaps in the ray coverage, especially toward the outer stations of the large-scale network (Text S5 and Figure S5 in Supporting Information S1).

In Section 3.1 above, the choice of discretization and hyper-parameters for a classical LET with one rather homogeneous data set is described. However, here two differently scaled data sets are available, distinguishable also in terms of ray coverage and density. Even if, in the end, the same ray paths are used to obtain a velocity model, the result is highly dependent on how these two data sets are merged and the parameter settings have to be chosen accordingly.

Various possibilities were tested to find an optimal way to combine the strengths each of the data sets offer. In a first straight forward approach, both data sets were inverted in one step, going directly from the 1D layered input model to a 3D high-resolution model. This led to a rather smooth model where the high amount of repeating ray paths of the large-scale data set (3,700 events) smooth out the high-resolution velocity anomalies that the temporary network (193 events) resolves.

Thus, a 2-step approach to combine the data sets was chosen where a first inversion of the long term data set obtains a rough velocity model, which is in turn used as an input velocity model for the inversion of the small-scale data set. It allows, if needed, to choose the regularization parameters separately for the different data sets, as well as speeding up the computation, since a coarser inversion and forward calculation grid can be chosen for the large-scale network, and a finer one for data of the small-scale network.

## 3.2.1. Parameter Setting for the Low-Resolution Model

Starting with the events and picks of the permanent stations and the layered 1D velocity model, the events are located with the probabilistic grid search algorithm NonLinLoc (NLL) (Lomax et al., 2000, 2009), and then those event locations, the picks, and the initial velocity model are used for retrieving a first low-resolution 3D velocity model with TomoTV (Latorre et al., 2004).

The greater the number of rays used to calculate the travel time tomography, the more robust the velocity model becomes. Thus, a low-resolution 3D model was calculated from a subset of the ÍSOR travel time picks from January 2021 to September 2022. Using only the 12 permanent stations keeps the computation time low, while taking advantage of the large amount of travel time picks. From these 3,700 events, a robust low-resolution 3D model is calculated with an inversion grid of 500 m spacing, a damping factor of 3 and laplacian smoothing in x and y direction of 0.5 and in z direction of 1. These parameter settings, except for the gridding, were used in all further inversions, since they also yielded the best results when combining the networks.

The velocity variations retrieved from the large-scale data set are quite smooth (Figure 3a), but differences in the velocity values are still substantial enough to highlight preliminary rough structures. Nevertheless large parts of the uppermost kilometer of the central volcano are not covered by rays and the velocity structures there can not be resolved.

## 3.2.2. Parameter Setting for the High-Resolution Model

The first low-resolution 3D model is in turn used as an input velocity model for locating the 193 picked events with the 98 nodes and the 12 stations. Computing the tomography with the data from the two networks running in parallel yields high-resolution 3D P- and S-wave velocity models. Also, for this second step, different ways of combining the two data sets are possible. Either the networks are used independently, where only the data of the

GLÜCK ET AL. 7 of 20

21699356, 2025, 5, Downloaded from https://agupubs.onlinelibrary.wiley.com/doi/10.1029/2024JB030425 by Ingv, Wiley Online Library on [11/11/2025]. See the Terms and Conditions (https://onlinelibrary.wiley.com/term/term)

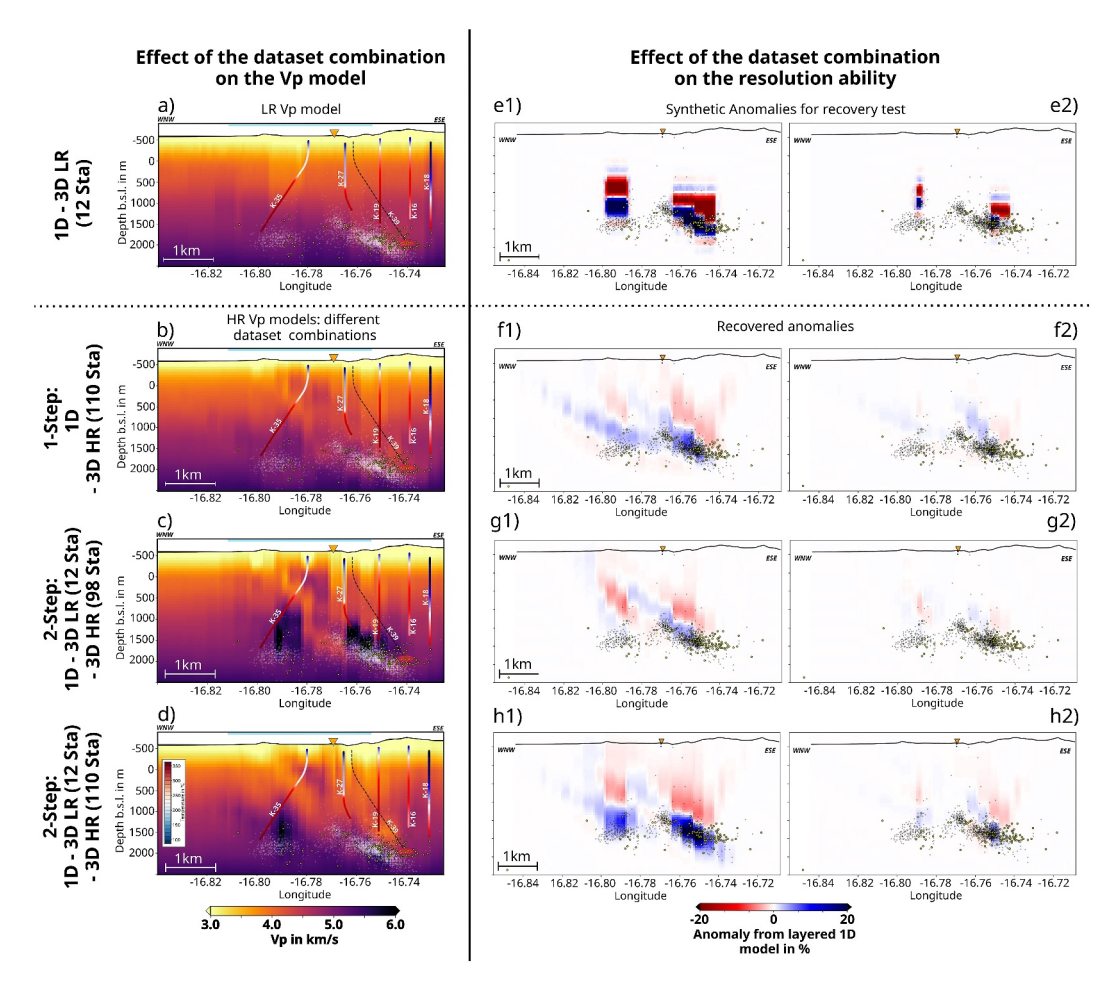


Figure 3. Resolution testing, cross-section along P1 of Figure 1: (a) Low-resolution (3D LR)  $V_P$  model, (b)  $V_P$  model from 1-step workflow (layered 1D directly to high-resolution 3D (3D HR)), (c)  $V_P$  model from 2-step workflow (layered 1D to 3D LR to 3D HR from 98 nodes), (d)  $V_P$  model from 2-step workflow (layered 1D to 3D LR to 3D HR from 12 Stations + 98 nodes), Resolution test: (e1) Synthetic anomalies: West— $2 \times 2 \times 2$  grid cells per positive/negative anomaly, East—2 grid cells in the latitude and step-shape in longitude direction, (e2), Synthetic anomalies: West— $1 \times 1 \times 1$  grid cell per positive/negative anomaly, East—1 grid cell in the latitude and step-shape in longitude direction, (f1) and (f2) recovered synthetic anomalies with the 1-step approach, (g1) and (g2) recovered synthetic anomalies with the 2-step approach (second step with 98 nodes), (h1) and (h2) recovered synthetic anomalies with the 2-step approach (second step with 98 nodes + 12 stations). The wells colored by formation temperature and seismicity (ÍSOR catalog in white, locations with the temporary network in yellow), are shown in the subfigures (a)—(d) for comparability with Figure 7.

98 nodes is taken to compute the high-resolution velocity model, or the data sets of both networks are combined for the events recorded during the period where both networks were running in parallel. The first possibility results in a velocity model that is de-coupled from the low-resolution model with very sharp velocity contrasts, which are not necessarily in accordance with the low-resolution model.

The latter option includes the permanent stations in the second step, where the temporary network is not used separately, but rather densifies the permanent network in the central part of the caldera during the time of experiment. This combination allows a better comparability of the low- and high-resolution models and an improved azimuthal station coverage. For the high-resolution model, inversion griddings of different cell size were tried. A grid spacing of 250 m seems the best choice, since structures sized within of the expected resolution are discretized appropriately, while keeping the computation time reasonable (L-curve and variation reduction: Text S7 and Figure S7 in Supporting Information S1).

GLÜCK ET AL. 8 of 20

Most of the velocity anomalies in the high-resolution model are larger than the theoretical maximum resolution according to the first Fresnel zone (600–1,000 m) (Section 3.1.1). However, we seem to be able to resolve smaller structures. To test the reliability of the resulting models and to check if there are differences in the resolution abilities of the various combination possibilities, a resolution test with differently sized anomalies (250 m–1 km) was performed for the 1-step and for both 2-step approaches with the low-resolution 3D model as initial velocity model and the re-located events as fixed sources (Figure 3). Synthetic anomalies (+/- 20% of  $V_p$  in the 1D layered model—Figures 3e1 and 3e2) were placed in areas where the strongest anomalies in the inverted high-resolution model were found. To keep the resolution test close to the anomalies found in the real data, the high velocity anomalies are overlain by low velocity anomalies, to check how much smearing might affect strong velocity contrasts.

The 1-step approach shows a high amount of smearing especially to the outer stations and thus little ability to recover the exact location of the small scale structures (Figures 3a, 3b, 3f1, and 3f2). The 2-step approach with the de-coupled data sets is not able to retrieve the lower high velocity anomaly in the same quality as the upper low velocity anomaly, since there are, due to the lack of remote stations, less rays traveling through the deeper parts (Figures 3c, 3g1, and 3g2). For the same reason most of the ray paths are oriented vertically, smoothing out the low and high velocity contrasts, especially for the small synthetic anomalies. When the two data sets are combined for the high-resolution imaging, the result still contains some smearing, but the anomalies and especially the velocity contrasts can be retrieved quite clearly, even for the small synthetic anomalies, due to the addition of the remote stations of the permanent network (Figures 3d, 3h1, and 3h2). This model is referred to in the following sections as the high-resolution 3D model.

## 3.3. Earthquake Location With Different Velocity Models

With the different velocity models that are now available, the layered 1D and the low-/high-resolution 3D models, the question arises, which of them should be used for locating earthquakes. The ability of the various models to reliably locate events with the different network settings is checked by comparing the mean residual at each station from running locations with NLL for the same event subset of June–July 2022 with the different velocity models and network configurations, where they can offer insights if velocities close to the stations are over- or underestimated. However, the station-wise residuals are generally used to apply a station correction on the location for which the mean station residual is subtracted from each pick time before re-running the location procedure to eliminate velocity structures close to the stations that are not included in the velocity model. Text S4/S6 and Figure S4/S6 in Supporting Information S1 gives details on the location process, the calculation of the RMS and station residuals.

## 3.3.1. Location With the Combined Permanent and Temporary Networks

Event picks always include a certain amount of noise from picking errors. If a high number of picks is used to determine a source location, these picking errors can lead to larger variations in the residuals. This seems to be the case here, where the histograms of the residuals for the 110 stations imply, that a more detailed velocity model does not lead to a reduction of the residuals. However, the station-wise residuals show that for the combined network, the high-resolution model does add information in the location process. The station residuals are lowest when the 3D high-resolution model is used (Figure 4 and Text S8 and Figure S8 in Supporting Information S1), and thus an application of a station correction will remove near-surface site effects instead of correcting for unresolved path effects as is the case for the less detailed models.

By using the 110 stations and the high-resolution model the location of the events is improved, even if the RMS and the histograms of the residuals seem to imply differently.

## 3.3.2. Location With the Permanent Network

Locating the same data set with only the 12 stations of the large-scale permanent network, the use of more detailed velocity models leads to a significant reduction of the residuals. As for the high- and low-resolution 3D velocity models, they both have much smaller but rather similar values for P-pick residuals compared to the layered 1D model (Text S8 and Figure S8 in Supporting Information S1). This similarity in the residuals for both 3D models

GLÜCK ET AL. 9 of 20

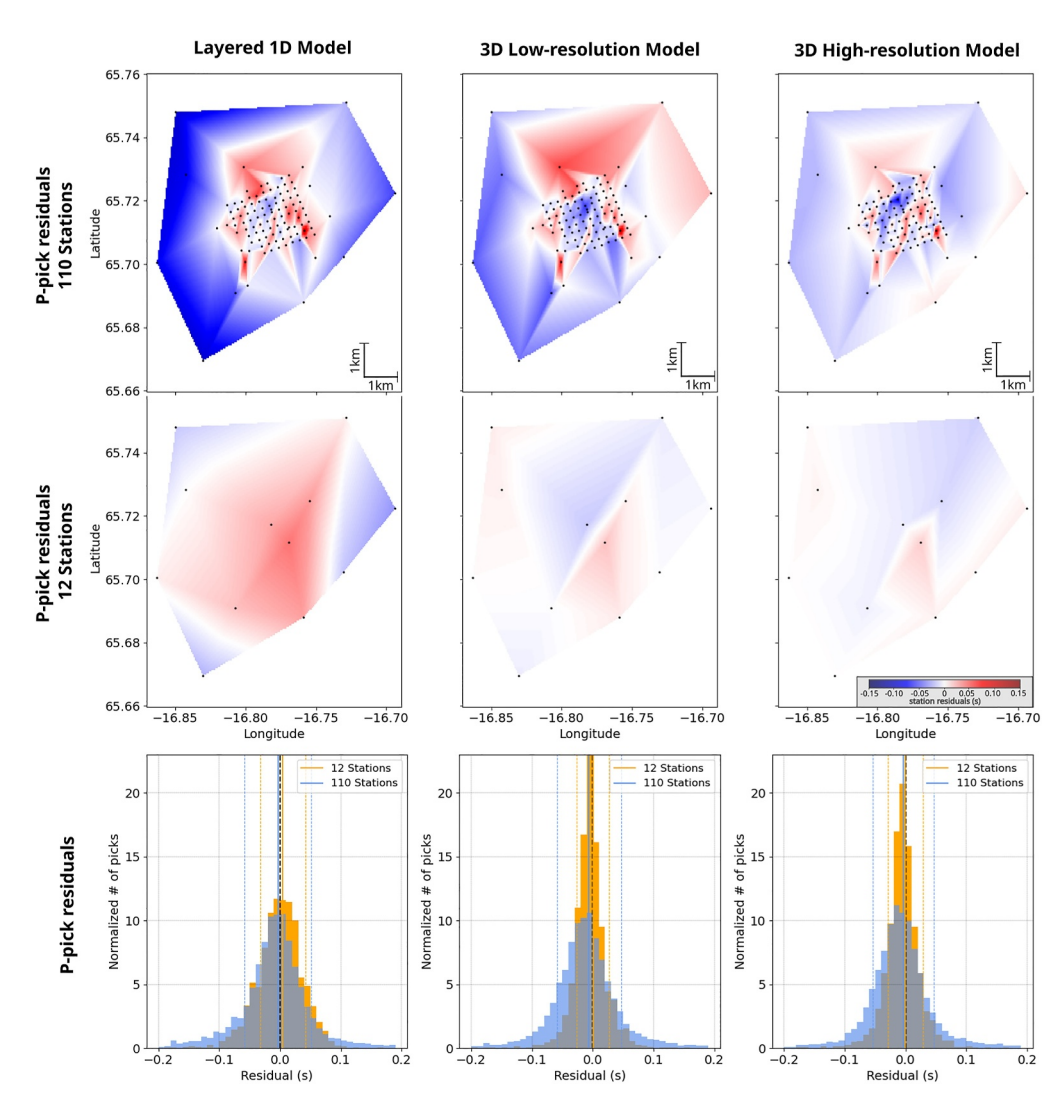


**Figure 4.** Station residuals for the different networks. Top row: Interpolated P-pick station residuals for the different input velocity models for the location with the ÍSOR data set. Middle row: Interpolated P-pick station residuals for the different input velocity models for the location with the combined 110 stations. Bottom row: Normalized distribution of all travel time residuals according to the velocity model for the 12 permanent (orange) and the combined 110 stations (blue). Dashed lines: standard deviation, black line: Zero residual.

can be explained by the fact that the 12 stations are not sensitive enough to the small-scale features that the high-resolution velocity model includes.

To monitor the seismicity over time with the permanent network, the 3D low-resolution model is chosen, because the residuals are slightly lower (Figure 4 and Text S8 and Figure S8 in Supporting Information S1), but also because the simpler of the two models that explains the data with the same accuracy is preferred. For imaging purposes, the temporary network adds valuable information that can not be resolved by the permanent network.

## 3.3.3. Monitoring Seismicity With the Permanent Network

Above, the residuals were used to determine how well each model performs the location of seismicity. Here, we compare the effect on the event locations for when the layered 1D model or the low-resolution 3D model is used, each with and without correcting for the station residual (Figure 5). The locations with the layered 1D velocity model without the station correction have a much higher RMS than the other location trials and the events are located about 300 m shallower. The station correction for the 1D model appears to have a similar effect on the RMS as using a 3D model, with the seismicity having a lower RMS and being shifted downwards. When using the

GLÜCK ET AL. 10 of 20

21699356, 2025, 5, Downloaded from https://agupubs.onlinelibrary.wiley.com/doi/10.1029/2024JB030425 by Ingv, Wiley Online Library on [11/11/2025]. See the Terms and Conditions (https://onlinelibrary.wiley.com/terms

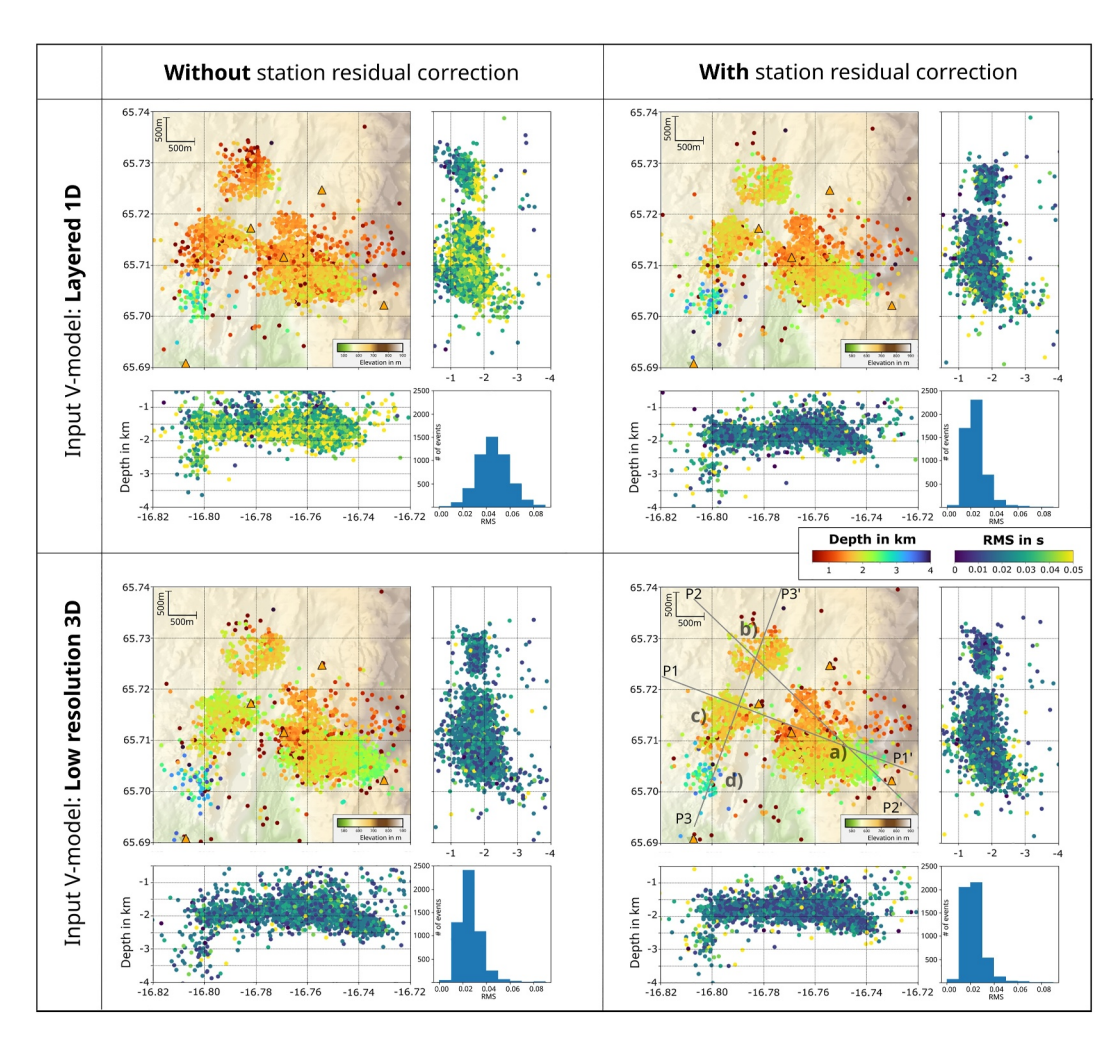


**Figure 5.** Earthquake locations (2021–2022) and RMS histograms for the layered 1D (top) and the low-resolution 3D (bottom) velocity models with (right) and without (left) station corrections. Bottom right panel: Final location of earthquakes in Krafla from 2021 to 2022, (a), (b), (c), and (d) refer to the different clusters of seismicity discussed in chapter 4.1. and P1–P3 mark the profiles shown in Figure 7.

low-resolution 3D model, the station correction does not affect the RMS or location much, except causing the seismicity pattern to be slightly less diffuse. Anyhow, the station corrected 3D background model is preferred to the station corrected layered 1D velocity model, since the correction applied to the 1D model removes mean path effects instead of near-surface anomalies. These however, are resolved in the 3D background model and the subtracted mean residuals are mainly due to unresolved near-surface site effects.

## 4. Results

## 4.1. Seismicity Pattern

The final locations of the events from 2021 to 2022 are calculated with the low-resolution 3D model and the 12 stations using picks corrected for the station residuals, with a mean horizontal and vertical error margin of 250 m. The seismicity can be divided into three main spatial clusters and a fourth smaller cluster (Figure 5). The largest and easternmost cluster is located 1–2.5 km b.s.l. (Figure 5, cluster a) with its lower NW–SE dipping boundary hosting the deepest seismicity almost 500 m deeper than in the center of the cluster. In the northern part, the deepest seismicity is at 1.5 km b.s.l.

There are two smaller clusters north (Figure 5, cluster b and c) and south of Leirhnjúkur, that are limited to the west by the Mývatn eruptive fissure and are only connected by minor seismicity to the eastern part. Both clusters

GLÜCK ET AL.

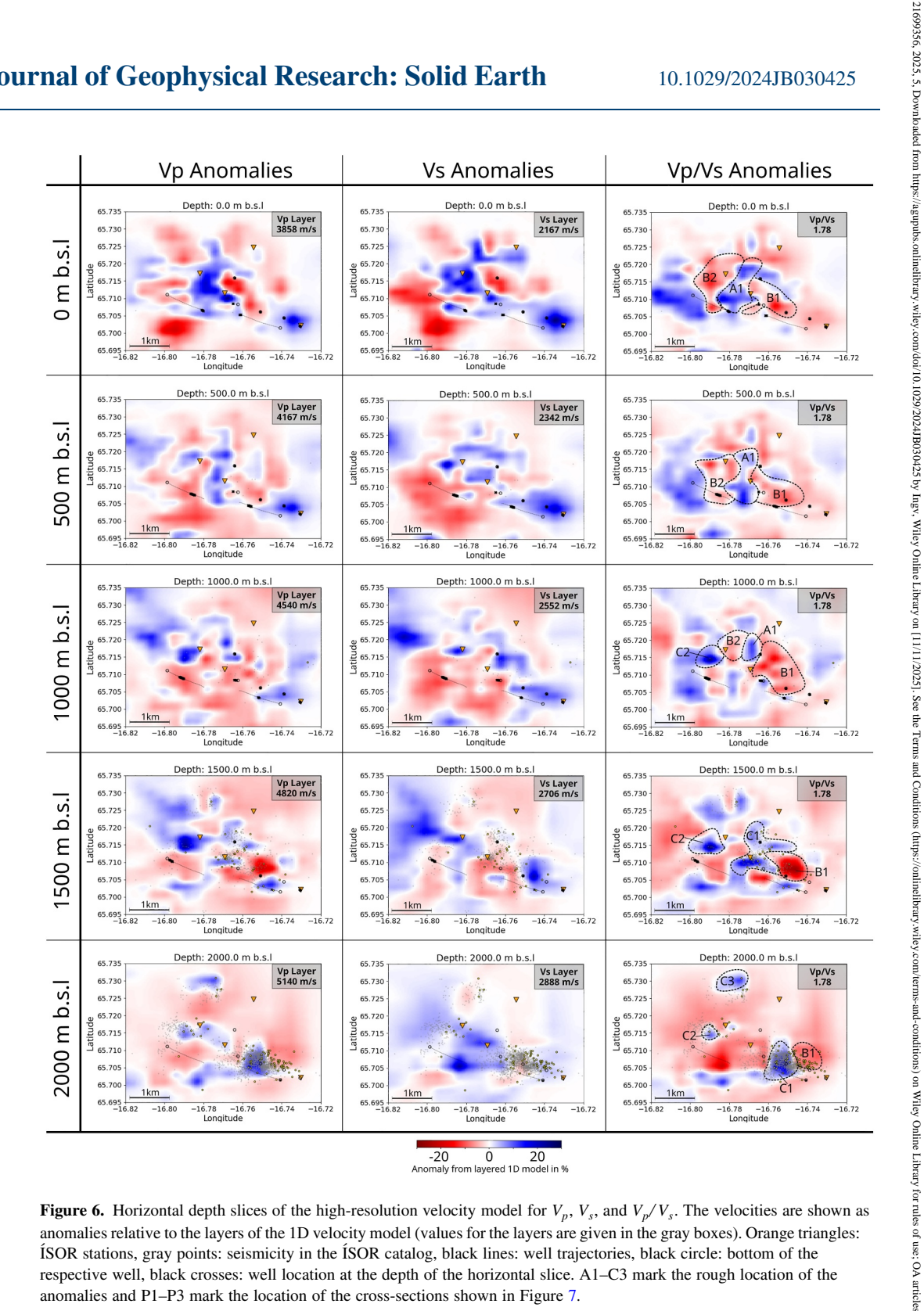


Figure 6. Horizontal depth slices of the high-resolution velocity model for  $V_p$ ,  $V_s$ , and  $V_p/V_s$ . The velocities are shown as anomalies relative to the layers of the 1D velocity model (values for the layers are given in the gray boxes). Orange triangles: ÍSOR stations, gray points: seismicity in the ÍSOR catalog, black lines: well trajectories, black circle: bottom of the respective well, black crosses: well location at the depth of the horizontal slice. A1-C3 mark the rough location of the anomalies and P1–P3 mark the location of the cross-sections shown in Figure 7.

are located from 1.4 km to almost 2 km b.s.l. with a seismically quiet zone between them. Cluster d is located south of c at depths of 2.5-4 km b.s.l.

## 4.2. Velocity Structures of the Multi-Scale Model

The obtained velocity structures of  $V_p$  and  $V_s$  show significant contrasts, ranging in the upper 2 km from 3,500 to 6,000 m/s for  $V_p$ , and from 1,500 to 3,500 m/s for  $V_s$  (Figures 6 and 7). The  $V_p/V_s$  ratio was not inverted

GLÜCK ET AL. 12 of 20

21699356, 2025, 5, Downloaded from https://agupubs.onlinelibrary.wiley.com/doi/10.1029/2024/B030425 by Ingv, Wiley Online Library on [11/11/2025]. See the Terms and Condi

ase; OA articles are governed by the applicable Creative Comm

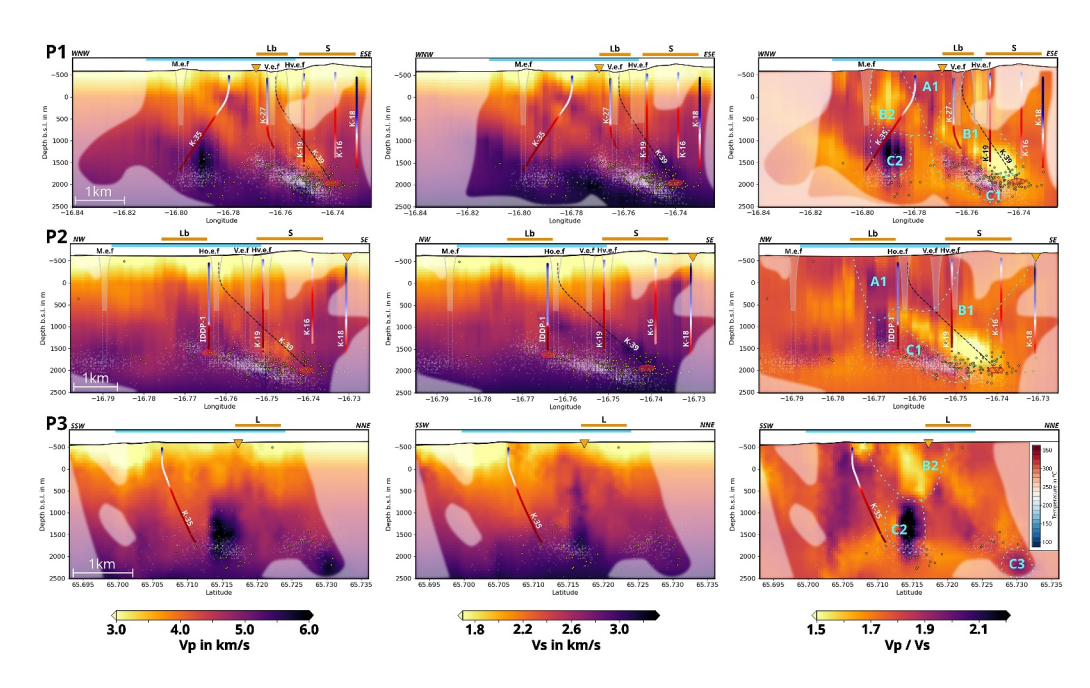


Figure 7. Cross-sections through the velocity models along with the formation temperature in nearby wells. The location of the profiles, wells, major eruptive fissures and L, Lb, S, and Vm are shown in Figure 1. The red ellipses indicate the points at which magma was encountered in IDDP-1 and K-39 wells. Yellow points show seismicity during the 2022 experiment that were used for the high-resolution tomography, gray points show the seismicity from 2021 to 2022. Orange triangles: ÍSOR stations, light blue line: extent of the temporary network. Note that the colorscale is different for each column of  $V_p$ ,  $V_s$ , and  $V_p/V_s$ .

separately, but was derived by dividing the two velocity models. Even though a smoothed model was used, it is possible that structures independently derived for P- and S-velocity models are not resolved with the same accuracy or exact location due to the sampling of the rays. This might induce some strong artificial contrasts in the  $V_p/V_s$  ratio. Therefore this has to be interpreted with care and always in comparison with the original  $V_p$  and  $V_s$  models.

Our models show several bodies with different velocity properties, their potential nature will be discussed later. They are grouped and numbered as A, B and C, according to their  $V_p/V_s$  ratio (Figures 6 and 7):

- A1—a north–south elongated high V<sub>p</sub> (and high V<sub>p</sub>/V<sub>s</sub>) structure located in the center of the caldera to the west
  of IDDP-1 at shallow depths. V<sub>s</sub> is also elevated in the whole area but not as localized as V<sub>p</sub>. In the southern
  part, the anomaly is cone-shaped and reaches almost 1 km b.s.l., while to the north, the anomaly is not as
  distinctly shaped and cuts off to the west almost vertically;
- B1 and B2—to east and west of A1, low  $V_p$  is dominating, while the  $V_S$  is not affected by this change, with the low  $V_p/V_s$  structure surrounding the high  $V_p/V_s$  cone. This low  $V_p$  zone is reaching almost 2 km b.s.l. in the Suðurhlíðar region, dipping toward the southeast. This results in a very pronounced low  $V_p/V_s$  ratio, as  $V_s$  increases in the same area;
- C1—a high  $V_p$  zone underneath the low velocity zone B1.  $V_s$  however is decreasing, leading to high  $V_p/V_s$  values:
- C2—a second high V<sub>p</sub> zone (up to 6 km/s) underneath Leirhnjúkur from 1 to 2 km b.s.l, about a kilometer wide, which V<sub>s</sub> is not sensitive to, resulting in high V<sub>p</sub>/V<sub>s</sub> values.
- C3—another high V<sub>p</sub> zone north of Leirhnjúkur that starts to appear from 2 km b.s.l, which V<sub>s</sub> is again not sensitive to. It is located at the edge of the area covered by rays.

GLÜCK ET AL. 13 of 20

## 5. Discussion

## 5.1. $V_p/V_s$ Behavior

What physical parameters in a geothermal system like the one at Krafla are likely to affect the  $V_p/V_s$  ratio? Assuming an elastic medium,  $V_p$  and  $V_s$  are defined by the bulk modulus  $\kappa$ , an inverse measure of the compressibility of a material, which itself depends on the density  $\rho$  and the shear modulus  $\mu$ , which is independent from  $\rho$  and equals zero in both gaseous and liquid fluids:

$$V_p = \sqrt{\frac{3\kappa + 4\mu}{3\rho}}$$
 and  $V_s = \sqrt{\frac{\mu}{\rho}}$  (1)

Higher densities are usually accompanied by higher bulk modulus, which increases  $V_p$ , while higher densities decrease  $V_s$ . For a porous rock saturated with fluids of different densities and compressibilities, the behavior of  $V_p$ ,  $V_s$  and  $V_p/V_s$  can give insights into the nature and phase of the fluid mixture.

If a rock is filled with gas, or if it is only partly saturated with liquid, the bulk modulus, and with it  $V_p$ , decreases, as gas is more compressible than liquid, while  $V_s$  increases slightly due to the lower density. However, in a volcanic area, liquids can be not only water or brine, but also magma, which has a higher bulk modulus than the former two. The same percentage of liquid present in a rock matrix, due to saturation with for example, water or due to partial melting, leads to very different velocities. With denser and less compressible fluids,  $V_p$  is higher in the presence of magma compared to water, while  $V_s$  is lowered.

This comparison allows to interpret the resulting  $V_p/V_s$  values accordingly. For gas saturated or dry rock,  $V_p/V_s$  is the lowest, while the presence of water or brine increases the ratio. Thus, a transition from steam to liquid should be a transition from low to high  $V_p/V_s$  (Ito et al., 1979). Values for  $V_p/V_s$  are highest in the presence of magma (Watanabe, 1993), which might also be of different composition than the surrounding rock in case of an intrusion, though in general, both velocities are lower in the presence of melt (Hammond & Humphreys, 2000; Poletto et al., 2018).

Temperature and pressure are the parameters that govern the phase of the fluids (Poletto et al., 2018). The boiling point curve (James, 1970) allows to evaluate when pure liquid, pure steam or 2-phase conditions are encountered. However, velocities of the rock matrix are also influenced by temperature and pressure; increasing temperature leads to a decrease in velocity, while increasing pressure has the opposite effect. In the following discussion, we neglect the influence that alteration or cementation might have on velocities.

## 5.2. Velocities Versus Well Log Data

#### 5.2.1. The Well Log Data

For Suðurhlíðar and Leirbotnar, in situ information is available, such as formation temperature data for a number of wells, along with lithology and alteration logs. In addition, mapped feed zones from Mortensen et al. (2014) for IDDP-1 can be used to robustly interpret our velocity models. The formation temperature logs displayed in Figure 8 are from wells IDDP-1, K-16, K-19, K-27, and K-35 (locations: Figure 1). In the cross-sections of Figure 7, the formation temperature for K-18 is also shown. For K-39, the other well that encountered magma during drilling, the well trajectory is shown. The boiling-point curve presented in Figure 8 is derived from in situ pressure measurements. There are difficulties to directly compare the very finely sampled log data with velocity values averaged over 250 m and limited by the resolution from the LET, not to mention that the wells are usually drilled across fissures (Mortensen et al., 2015) that are also boundaries in the velocity structures. However, the major changes in the logs can be associated to our observed velocity changes (Figure 8) allowing a more robust interpretation of the imaged structures.

## 5.2.2. The Relationship of Seismic Velocities and Temperature at Krafla

The phase of fluids present in the rock matrix at Krafla is likely to affect the seismic velocities. From the comparison of the high-resolution velocity models with the formation temperatures and the boiling point curves, a qualitative description of the velocity-temperature relationship can be approached. Since there are either single-

GLÜCK ET AL. 14 of 20

21699356, 2025, 5, Downloaded from https://agupubs.onlinelibrary.wiley.com/doi/10.1029/2024JB030425 by Ingv, Wiley Online Library on [11/11/2025]. See the Terms

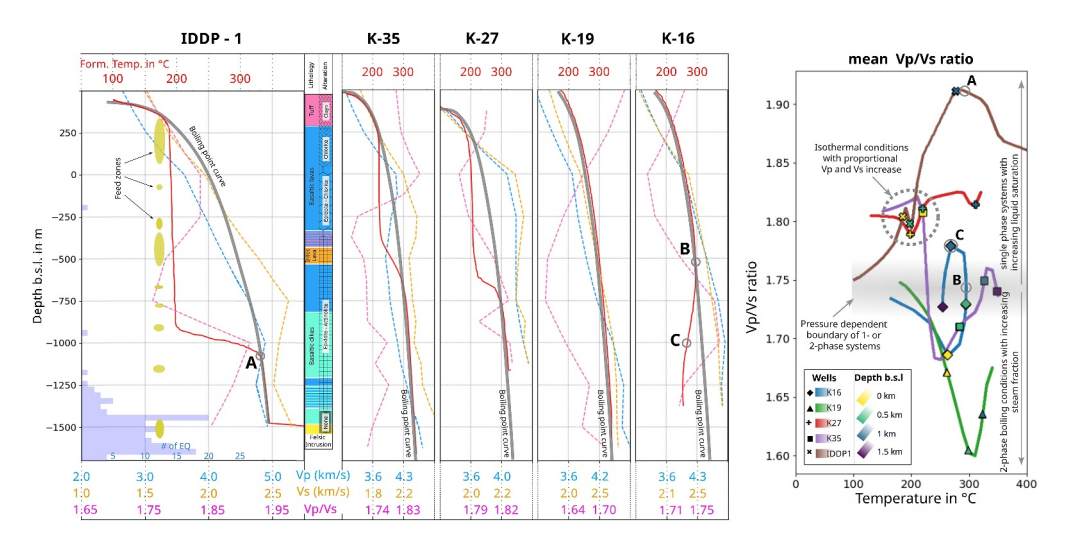


Figure 8. Well logs versus model velocities: Left: Well logs with formation temperature in red (for IDDP-1 only starting 112 m below the well head), theoretical boiling point curve (black) and the velocities ( $V_P$ —blue,  $V_S$ —yellow,  $V_P/V_S$ —pink) of the high-resolution model along the wells and for IDDP-1 including the depth of the nearby relocated seismicity (blue histogram), lithology, alteration and mapped feed zones from Mortensen et al. (2014). Right: Behavior of formation temperature with  $V_P/V_S$  for the different wells. The markers, different for each well, show the depth dependence of the temperature-velocity relation.

phase liquid or 2-phase boiling conditions present, these wells can be used to interpret the velocities according to the fluid phase present in the rock matrix.

Point A in Figure 8 marks the transition from single phase liquid to boiling conditions, after which the steam fraction in IDDP-1 increases with depth. This transition results in a decrease of  $V_p/V_s$ , due to a lower bulk modulus of steam compared to liquid. Point B in Figure 8 marks the opposite transition toward the liquid phase in K-16, resulting in increasing velocities. With the assumption that the saturation remains similar, while the lower temperature only allows for single phase liquid conditions, the increase of  $V_p/V_s$  is most likely due to a higher bulk modulus. However, from point C, K-16 encounters almost isothermal conditions and decreasing  $V_p/V_s$  ratios, possibly due to decreasing fluid saturation.

Thus, decreasing  $V_p/V_s$  values might be related to a decrease or absence of liquid phase fluids, due to a higher fraction of steam in a 2-phase system, or simply a lower degree of saturation. High and increasing  $V_p/V_s$  values can be attributed to an increase in liquid phase. This can be attributed to low temperatures, as it is the case for the isothermal zone, for example, in IDDP-1, or to increasing pressure that allows for a higher fraction of liquid phase in a 2-phase system.

# 5.2.3. High $V_p/V_s$ Zones and Low Temperature Conditions

Region A1 (Figures 6 and 7) has an increased  $V_p/V_s$  ratio due to elevated  $V_p$ . It suggests the presence of a saturated zone with liquid phase fluids, which is consistent with the mapped feed zones in this area (Figure 8, IDDP-1 log) (Mortensen et al., 2014). The formation temperature logs from wells IDDP-1, K-27 and K-35 show isothermal conditions beneath the boiling-point when crossing the area of A1, which can also be observed in the temperature-velocity relationship. The proportional increase of  $V_p$  and  $V_s$  leads to constant, higher  $V_p/V_s$  values between 1.80 and 1.83, characterizing A1.

Based on the alteration degree of basalts encountered in A1 by various wells (e.g., IDDP-1 in Figure 8), Árnason (2020) suggests that the isothermal part of the system must have cooled down from once boiling conditions, probably due to an increase in permeability generated during rifting episodes. We can therefore assume that within A1, the high permeability in the direction of the fissure swarm favors isothermal conditions in the system. The high  $V_p$  within A1 can thus be a result of cooler water circulating in the more permeable layers down to almost 1,000 m b.s.l.

GLÜCK ET AL. 15 of 20

21699356, 2025, 5, Downloaded from https://agupubs

## 5.2.4. Low $V_p/V_s$ Zones and High Temperature Conditions

When wells are drilled in boiling conditions, like K-19, the upper part of K-16, and the lower part of K-35, the temperature-velocity relationship (Figure 8) depends mainly on the liquid phase saturation and depth (pressure). All those wells exhibit a similar behavior. First,  $V_p/V_s$  is decreasing with depth, indicating an increasing steam fraction in the boiling conditions, which is highest where the  $V_p/V_s$  ratio reaches its minimum. With increasing depth and pressure, the liquid phase fraction becomes more dominant again, presumably resulting in a rise of  $V_p/V_s$ . Even though the velocity-temperature pattern is similar for those wells, the values vary, which could be explained by differing saturation degrees, or to a smaller extent by changes of the lithology and fracturation (Gritto et al., 2023).

The zones of B1 and B2 exhibit a low  $V_p/V_s$  ratio due to low  $V_p$ , an indicator for the existence of a 2-phase or even single vapor phase fluid, similar to the steam zones found at the geothermal fields of the Geysers and Lardarello (De Matteis et al., 2008; Delliansyah et al., 2015; Gunasekera et al., 2003). This can be interpreted as upflow zones of the geothermal system. The formation temperature in well IDDP-1 reaches boiling conditions at the same depths at which  $V_p/V_s$  is starting to decrease, at around 1 km b.s.l., as the well reaches B1 in the Leirbotnar geothermal sub-field. At Suðurhlíðar, evidence of the geothermal system can be observed at the surface with high temperatures and degassing (Bini et al., 2024). The velocity-temperature behavior of K-19 supports that boiling conditions with different amounts of steam and liquid fractions are encountered from the surface on, which are characteristic for B1. The eastern boundary of B1 could be imaged through increasing  $V_p/V_s$  values at depths. It corresponds to the formation temperature reversal and phase transition observed at K-16 at 500 m b.s.l. (Figure 8). Well K18, even further east, is already outside of B1 with colder temperatures.

For the western geothermal field, at Leirhnjúkur, there is no well data available, except the lower part of K-35, which is deviated westwards from Leirbotnar to the south of Leirhnjúkur. After crossing the isothermal zone of A1, K-35 exhibits the same behavior of  $V_p/V_s$  for boiling conditions as for example, K-19 (Figure 8). With B2 having similarly low  $V_p/V_s$  values as B1 and being located underneath geothermal surface manifestations with high surface temperatures (Bini et al., 2024) (Profile 1 and 3 in Figure 7), boiling conditions are expected at Leirhnjúkur from the surface down to 1 km b.s.l., similar to the upflow system at Suðurhlíðar.

## 5.2.5. High $V_p/V_s$ Zones and High Temperature Conditions

Beneath B1 and B2, high  $V_p/V_s$  ratios with extremely high  $V_p$  values, are encountered in the zones C1, C2, and more to the north at the edge of the ray coverage, C3 (Figure 7). With such a high bulk and rather low shear modulus, these anomalies might be the signature of magma batches acting as a heat source for the upflow systems B1 and B2. For instance at Akutan volcano in Alaska, Koulakov et al. (2021) interpreted high  $V_p/V_s$  beneath low  $V_p/V_s$  zones as magmatic chambers underlying possible steam zones. The C2 and C3 zones at Krafla have not been drilled into, but IDDP-1 and K-39 reached at least the vicinity of the C1 zone. These in situ observations strengthen the interpretation of very high  $V_p/V_s$  in volcanic areas as an indicator of magma batches.

## 5.3. Active Structures and Upflow Zones

The main cluster of seismicity seems to be located at the upper boundary of C1, where it is partly within the high  $V_p/V_s$  area that is possibly linked to magma and therefore a ductile area. This apparent contradiction could be explained by the limited precision in earthquake locations, or by the existence of small lenses of magma rather than large magma batches. In Leirbotnar, IDDP-1 encountered magma at 2.1 km depth, where high  $V_p$  values are observed. However, the  $V_p$  and  $V_p/V_s$  values are not as high as they are in the Suðurhlíðar region, therefore the velocity signature of the magma sampled by the IDDP-1 well is averaged out and can not be resolved with LET.

It was already suggested by Schuler et al. (2016) that the shallower seismicity around IDDP-1 is located above the magma batch encountered during drilling. Considering the horizontal and vertical location error of 250 m of the seismic events presented here, this suggestion remains plausible, since the main seismicity around IDDP-1 ranges between 1,400 and 1,600 m b.s.l. (Figure 7).

Well K-39 was drilled into magma south-east of zone C1 at 2.6 km depth (Figure 7, Profiles 1 and 2). The magma was found just outside our ray coverage, so no velocity values are available in this region. However, if the lines of

GLÜCK ET AL. 16 of 20

21699356, 2025, 5, Downloaded from https

onlinelibrary.wiley.com/doi/10.1029/2024JB030425 by Ingv, Wiley Online Library on [11/11/2025].

high  $V_p$  gradient observed in Profiles 1 and 2 are extrapolated, they meet the bottom point of K-39. Just as for IDDP-1, the seismicity is located at similar levels as the encountered magma.

If the melts encountered by wells IDDP-1 and K-39 have a common source, as suggested by the geochemical analysis of the rock samples (Rule, 2020), the southeast dipping seismicity aligning with the steep, also southeast dipping gradient of  $V_p$  could outline the boundary of a magmatic intrusion or an area hosting multiple magma batches acting as a heat source for the upflow system located underneath Suðurhlíðar and Leirbotnar.

For the western geothermal field, Profiles 1 and 3 in Figure 7 show that the seismicity is not located above the heat source as is the case in the eastern part, but below the C2 structure. Assuming that magma was emplaced there as a batch or sill, it may be thin enough to create conditions for brittle failure underneath. In contrast to the eastern part, the boundary separating C2 and B2 is seismically quiet. This might be due to different stress conditions and/or the fact that this potential heat source and upflow zone is not utilized for geothermal energy production. This suggests that the mechanisms triggering seismicity are different at Leirhnjúkur from the ones at Suðurhlíðar or Leirbotnar.

#### 5.4. Comparison With the Previously Available Velocity Model

The comparison of the seismicity and velocity model presented in Schuler et al. (2015) and the results from the high-resolution models presented here for the central area of the Krafla caldera lead to different or even contradicting interpretations. Since the well data are in situ measurements, they are the key for interpreting the velocity structures in the models. Both models show alternating low and high  $V_p/V_s$  areas with depth though they, just as the depth of the seismicity, seem to be shifted downwards 500–1,000 m in Schuler et al. (2015), leading to a different association of in situ measurements with the velocity values in the models. The main difference is, that in the velocity model presented here, the sampled magma batches are in the vicinity of very high  $V_p/V_s$  areas, while in the previously published model they are located above very low  $V_p/V_s$  areas. This shift might be attributed to an overestimation of the velocities in the upper central part of the geothermal system in Schuler et al. (2015), that can now be resolved better with the high-resolution velocity model presented here. However, the previous velocity model, though with less resolution, extends well beyond the caldera boundaries, unlike the ones presented here. Thus, the models can be seen as complementary and merging the data sets, similar to the workflow used for this study which might make the results more comparable.

## 6. Conclusion

## 6.1. Different Network Combinations for Different Purposes

The permanent large-scale and the temporary small-scale seismic networks running in parallel enabled us to use the two data sets, depending on the purpose, either together or separately. For both networks, the same workflow was applied, resulting in comparable low- and high-resolution  $V_p$  and  $V_s$  models.

For both aims, that is, structural imaging and seismic event location, the event- and station-wise residuals were considered. To relocate the seismicity from the ISOR catalog a combination of the low-resolution velocity model and the picks from 12 permanent stations is chosen, since it does not include velocity structures that the permanent network is insensitive to.

However, the high-resolution velocity model obtained from the combined networks performs the relocation better than the low-resolution model does with 110 stations, and is thus considered more reliable in terms of structural imaging.

For an optimal network design for future multi-scale experiments, better results could probably be obtained by considering how the permanent network can contribute in the most efficient way. In the target region, a high density of stations is useful, but both networks should be linked with a number of stations to avoid gaps in the station coverage, particularly for remote permanent stations.

## 6.2. High-Resolution Structural Imaging of Krafla

The results of the LET and seismicity together with the additional well log data allow a comprehensive study of velocity structures at the center of Krafla caldera at scales of 250–500 m.

GLÜCK ET AL. 17 of 20

21699356, 2025, 5, Downloaded from https://agupubs.onlinelibrary.wiley.com/doi/10.1029/2024JB030425 by Ingv, Wiley Online Library on [11/11/2025]. See the Terms

The comparison of available well log data and the obtained velocity model shows that the main reason for velocity variations is not so much due to lithology, but rather the (anisotropic) permeability, the saturation degree and the phase/composition of the fluid. The eastern and western geothermal fields at Krafla each have an upflow system at boiling conditions (low  $V_p/V_s$ ) with varying fractions of steam and liquid reaching the surface. They are separated by a boundary structure, characterized by higher  $V_p$  and lower temperatures, the result of a higher permeability allowing the inflow of colder fluids.

Both upflow zones seem to have distinct heat sources (high  $V_p/V_s$ ), that could be of magmatic origin. The one beneath Leirhnjúkur is located at shallower depths than the one beneath Suðurhlíðar and Leirbotnar, which is dipping downwards from 1.5 to 2.2 km b.s.l. in the southeast direction, triggering seismicity at its upper boundary. Two wells, IDDP-1 and K-39 encountered magma during drilling close to where a dipping continuous high  $V_p/V_s$  structure was imaged, indicating that the same magma source might have been sampled.

## 6.3. Outlook

For gaining a better understanding of the velocity structures in the upper layers of Krafla, imaging by ambient noise tomography can be considered. Depending on the quality of the cross-correlations, a surface wave velocity model might yield more insights on near-surface structures. By using not only local earthquakes or ambient noise, but the whole waveform, waveform equation tomography or even full waveform inversion could help image subsurface structures in more detail.

However, to interpret any tomographic result on seismic velocities at Krafla, other imaging methods should be included in the interpretation to remove ambiguities. Within the MSCA-IMPROVE project, magnetotelluric, electrical resistivity, gravity and geochemical data are available. By jointly interpreting the results, the conceptual model of Krafla might become more robust. Modeling those parameters may also allow for a more quantitative understanding of their relationship with temperature, pressure, saturation and fluid phase.

The 10-year earthquake catalog from ÍSOR offers the opportunity to track changes in the seismicity patterns over time. Combining this with tracking changes of seismic velocities in sub-fields of the geothermal system, as well as changes in the stress field and seismicity patterns can improve our understanding of how Krafla is evolving over time due to internal processes like inflation/deflation or external factors like regional seismicity or anthropogenic influences from geothermal utilization.

## **Data Availability Statement**

Cut-out waveforms (7 s snippets in.mseed format) of the seismic events used in this study and the manually picked traveltimes of the nodal array along with the code designed to compute the NonLinLoc input files and the Wadati diagram (for a fast quality check of the picks) are made available in Glück et al. (2024). The formation temperature was published in Berthet et al. (2016). Software: Onset picking: Pyrocko application Snuffler (Heimann et al., 2017). Earthquake localization: NonLinLoc (Lomax et al., 2000, 2009). LET: TomoTV (Virieux et al., 2015). Maps were created with GMT5 (Wessel et al., 2013).

## References

Ármannsson, H., Gudmundsson, A., & Steingrímsson, B. (1987). Exploration and development of the Krafla geothermal area. *Jökull Journal*, 37(1), 13–30. https://doi.org/10.33799/jokull1987.37.013

Árnason, K. (2020). New conceptual model for the magma-hydrothermal-tectonic system of Krafla, NE Iceland. Geosciences, 10(1), 34. https://doi.org/10.3390/geosciences10010034

Arnott, S., & Foulger, G. (1994). The Krafla spreading segment, Iceland: 1. Three-dimensional crustal structure and the spatial and temporal distribution of local earthquakes. *Journal of Geophysical Research*, 99(B12), 23801–23825. https://doi.org/10.1029/94jb01465

Bagagli, M., Kissling, E., Piccinini, D., & Saccorotti, G. (2020). Local earthquake tomography of the larderello-travale geothermal field. Geothermics, 83, 101731. https://doi.org/10.1016/j.geothermics.2019.101731

Berthet, J.-C., Guðmundsdóttir, V., Þorgilsson, G., & Andri, A. (2016). Simulation of the Krafla geothermal system, resource assessment of shallow peripheral zones [Dataset]. 16.02, ÍSOR-2016/011. Prepared by Iceland GeoSurvey (ISOR) and Vatnaskil for Landsvirkjun (LV). https://gogn.lv.is/files/2016/simulation\_of\_krafla\_geothermal\_system.pdf

Bini, G., Chiodini, G., Ricci, T., Sciarra, A., Caliro, S., Mortensen, A., et al. (2024). Soil CO<sub>2</sub> emission and stable isotopes (δ<sup>13</sup>C, δ<sup>18</sup>O) of CO<sub>2</sub> and calcites reveal the fluid origin and thermal energy in the supercritical geothermal system of Krafla, Iceland. *Journal of Volcanology and Geothermal Research*, 447, 108032. https://doi.org/10.1016/j.jvolgeores.2024.108032

Bodvarsson, G., Pruess, K., Stefansson, V., & Elíasson, E. T. (1984). The Krafla geothermal field, Iceland: 2. The natural state of the system. Water Resources Research, 20(11), 1531–1544. https://doi.org/10.1029/wr020i011p01531

Brandsdóttir, B., Menke, W., Einarsson, P., White, R. S., & Staples, R. K. (1997). Färoe-Iceland ridge experiment 2. Crustal structure of the Krafla central volcano. *Journal of Geophysical Research*, 102(B4), 7867–7886. https://doi.org/10.1029/96jb03799

# Acknowledgments

This study received funding from the European Union's Horizon 2020 research and innovation program No. 858092 (IMPROVE project). For making available the data and also for the logistical support provided during the fieldwork, we would like to acknowledge Landsvirkjun and ÍSOR. This study would not have been possible without the support in the field from Laurent Métral, Baptiste Camus, Sandrine Roussel, Lydie Gailler, Maurice Weber, Regina Maass and other IMPROVE ESRs, who helped deploying the nodes for the seismic experiment. Thanks also to Sylia Benchabane for her help with the onset picking during her internship and to Ana Martinez Garcia for providing a ready-to-use DEM. The manuscript was also greatly improved by the comments of the editor and the two reviewers

GLÜCK ET AL.

- Buijze, L., van Bijsterveldt, L., Cremer, H., Jaarsma, B., Paap, B., Veldkamp, H., et al. (2019). Induced seismicity in geothermal systems: Occurrences worldwide and implications for The Netherlands. In *European geothermal congress* (pp. 11–14).
- Delliansyah, R., Sule, R., & Nugraha, A. D. (2015). Steam and brine zones prediction inside an operated geothermal reservoir based on seismic velocities produced by double difference tomography. In World geothermal congress (pp. 1–4).
- De Matteis, R., Vanorio, T., Zollo, A., Ciuffi, S., Fiordelisi, A., & Spinelli, E. (2008). Three-dimensional tomography and rock properties of the Larderello-Travale geothermal area, Italy. *Physics of the Earth and Planetary Interiors*, 168(1–2), 37–48. https://doi.org/10.1016/j.pepi.2008.
- Einarsson, P. (1978). S-wave shadows in the Krafla caldera in NE-Iceland, evidence for a magma chamber in the crust. *Bulletin Volcanologique*, 41(3), 187–195. https://doi.org/10.1007/bf02597222
- Einarsson, P. (1991). Umbrotin við kröflu 1975-89. In A. Garðarsson & Á. Einarsson (Eds.), Náttúra mývatns (pp. 97–139). Hið íslenska náttúrufræðifélag.
- Einarsson, P., & Brandsdóttir, B. (2021). Seismicity of the northern volcanic zone of Iceland. Frontiers in Earth Science, 9, 628967. https://doi.org/10.3389/feart.2021.628967
- Elíasson, E. T., Sverrir, T., & Steingrímsson, B. (2014). Geothermal power plants. In Short course VI on utilization of low- and medium-enthalpy geothermal resources and financial aspects of utilization. UNU GTP.
- Flóvenz, Ó. G., Ágústsson, K., Guðnason, E. Á., & Kristjánsdóttir, S. (2015). Reinjection and induced seismicity in geothermal fields in Iceland. In *Proceedings world geothermal congress* (pp. 19–25).
- Glück, E., Garambois, S., Vandemeulebrouck, J., Virieux, J., Muzellec, T., Gudnason, E. A., & Agustsdottir, T. (2024). Seismicity patterns and multi-scale imaging of Krafla (N-E) Iceland with local earthquake tomography: Raw event waveforms for all events used in the inversion and manual picks for temporary network [Dataset]. Zenodo. https://doi.org/10.5281/zenodo.15166137
- Gritto, R., Jarpe, S. P., Hartline, C. S., & Ulrich, C. (2023). Seismic imaging of reservoir heterogeneity using a network with high station density at the geysers geothermal reservoir, CA, USA. *Geophysics*, 88(5), WB11–WB22. https://doi.org/10.1190/geo2022-0490.1
- Gunasekera, R. C., Foulger, G. R., & Julian, B. R. (2003). Reservoir depletion at the geysers geothermal area, California, shown by four-dimensional seismic tomography. *Journal of Geophysical Research*, 108(B3). https://doi.org/10.1029/2001jb000638
- Guðnason, E. Á., Ágústsdóttir, Þ., Magnussón, R. L., & Gunnarsson, K. (2023). Seismic monitoring in Krafla, Þeistareykir and námafjall. reprocessing of the entire 2006-2022 catalogue. Report no. LV-2023-021. Prepared by Iceland GeoSurvey (ISOR) for Landsvirkjun (LV).
- Hammond, W. C., & Humphreys, E. D. (2000). Upper mantle seismic wave velocity: Effects of realistic partial melt geometries. *Journal of Geophysical Research*, 105(B5), 10975–10986. https://doi.org/10.1029/2000jb900041
- Hansen, P. C. (1999). The 1-curve and its use in the numerical treatment of inverse problems.
- Heimann, S., Kriegerowski, M., Isken, M., Cesca, S., Daout, S., Grigoli, F., et al. (2017). Pyrocko An open-source seismology toolbox and library [Software]. gfz data services. https://doi.org/10.5880/GFZ.2.1.2017.001
- Husen, S., Kissling, E., Deichmann, N., Wiemer, S., Giardini, D., & Baer, M. (2003). Probabilistic earthquake location in complex three-dimensional velocity models: Application to Switzerland. *Journal of Geophysical Research*, 108(B2). https://doi.org/10.1029/2002jb001778
  Ito H. DeVilbiss, J. & Nur. A. (1979). Compressional and shear waves in saturated rock during water-steam transition. *Journal of Geophysical*
- Ito, H., DeVilbiss, J., & Nur, A. (1979). Compressional and shear waves in saturated rock during water-steam transition. *Journal of Geophysical Research*, 84(B9), 4731–4735. https://doi.org/10.1029/jb084ib09p04731
- Johannesson, H., & Saemundsson, K. (1998a). Geological map of Iceland, 1:500,000, bedrock. Icelandic Institute of National History. Johannesson, H., & Saemundsson, K. (1998b). *Geological map of Iceland, 1:500,000, tectonics*. Icelandic Institute of National History.
- Johannesson, H., & Saemundsson, K. (1998). Geological map of Iceland, 1:1,000,000. Icelandic Institute of National History.
- Kim, D., Brown, L. D., Árnason, K., Gudmundsson, Ó., Ágústsson, K., & Flóvenz, Ó. G. (2020). Magma "bright spots" mapped beneath Krafla, Iceland, using RVSP imaging of reflected waves from microearthquakes. *Journal of Volcanology and Geothermal Research*, 391, 106365. https://doi.org/10.1016/j.jvolgeores.2018.04.022
- Kissling, E., Ellsworth, W., Eberhart-Phillips, D., & Kradolfer, U. (1994). Initial reference models in local earthquake tomography. *Journal of Geophysical Research*, 99(B10), 19635–19646. https://doi.org/10.1029/93jb03138
- Koulakov, I., Jakovlev, A., & Luehr, B. G. (2009). Anisotropic structure beneath central java from local earthquake tomography. *Geochemistry*, *Geophysics*, *Geosystems*, 10(2). https://doi.org/10.1029/2008gc002109
- Koulakov, I., Komzeleva, V., Smirnov, S. Z., & Bortnikova, S. B. (2021). Magma-fluid interactions beneath Akutan volcano in the Aleutian arc based on the results of local earthquake tomography. *Journal of Geophysical Research: Solid Earth*, 126(3), e2020JB021192. https://doi.org/10.1029/2020jb021192
- Latorre, D., Virieux, J., Monfret, T., Monteiller, V., Vanorio, T., Got, J.-L., & Lyon-Caen, H. (2004). A new seismic tomography of Aigion area (Gulf of Corinth, Greece) from the 1991 data set [Software]. *Geophysical Journal International*, 159(3), 1013–1031. https://doi.org/10.1111/j. 1365-246x.2004.02412.x
- Lee, B., Unsworth, M., Árnason, K., & Cordell, D. (2020). Imaging the magmatic system beneath the krafla geothermal field, Iceland: A new 3-d electrical resistivity model from inversion of magnetotelluric data. *Geophysical Journal International*, 220(1), 541–567. https://doi.org/10.1093/gji/ggz427
- Li, C., & Duric, N. (2013). Resolution limitation of travel time tomography: Beyond the first Fresnel zone. Medical imaging 2013: Ultrasonic imaging, tomography, and therapy, 8675, 359–368.
- Lin, G., & Wu, B. (2018). Seismic velocity structure and characteristics of induced seismicity at the geysers geothermal field, eastern California. *Geothermics*, 71, 225–233. https://doi.org/10.1016/j.geothermics.2017.10.003
- Lomax, A., Michelini, A., & Curtis, A. (2009). Earthquake location, direct, global-search methods [Software]. In R. A. Meyers (Ed.), Encyclopedia of complexity and systems science (pp. 1–33). Springer New York. https://doi.org/10.1007/978-3-642-27737-5\_150-2
- Lomax, A., Virieux, J., Volant, P., & Berge-Thierry, C. (2000). Probabilistic earthquake location in 3D and layered models: Introduction of a metropolis-Gibbs method and comparison with linear locations [Software]. In Advances in seismic event location (pp. 101–134). https://doi.org/10.1007/978-94-015-9536-0
- Mortensen, A., Egilson, P., Gautason, B., Árnadóttir, S., & Guðmundsson, Á. (2014). Stratigraphy, alteration mineralogy, permeability and temperature conditions of well IDDP-1, Krafla, NE-Iceland. *Geothermics*, 49, 31–41. https://doi.org/10.1016/j.geothermics.2013.09.013
- Mortensen, A., Grönvold, K., Gudmundsson, Á., Steingrímsson, B., & Egilson, T. (2010). Quenched silicic glass from well KJ-39 in Krafla, North-Eastern Iceland. In World geothermal congress (pp. 1–6).
- Mortensen, A., Guðmundsson, Á., Steingrímsson, B., Sigmundsson, F., Axelsson, G., Ármannsson, H., et al. (2015). *The Krafla geothermal system research summary and conceptual model revision* (Tech. Rep. No. LV-2015-098). Landsvirkjun.
- Mossop, A. P. (2001). Seismicity, subsidence and strain at the geysers geothermal field (PhD thesis). Stanford University, Department of Geophysics.

GLÜCK ET AL. 19 of 20

- Poletto, F., Farina, B., & Carcione, J. M. (2018). Sensitivity of seismic properties to temperature variations in a geothermal reservoir. Geothermics, 76, 149–163. https://doi.org/10.1016/j.geothermics.2018.07.001
- Ragnarsson, A., Steingrímsson, B., & Thorhallsson, S. (2023). Geothermal development in Iceland 2020–2022. In *Proceedings of the world geothermal congress* (pp. 15–17).
- Reiser, F., Schmelzbach, C., Sollberger, D., Maurer, H., Greenhalgh, S., Planke, S., et al. (2020). Imaging the high-temperature geothermal field at Krafla using vertical seismic profiling. *Journal of Volcanology and Geothermal Research*, 391, 106474. https://doi.org/10.1016/j.jvolgeores. 2018.10.019
- Rule, G. (2020). The origin of magma encountered during drilling of geothermal well KJ-39, Krafla, Iceland and the relationship with the nearby IDDP-1 magma.
- Sæmundsson, K. (1991). Geology of the Krafla system. The Natural History of Lake Myvatn, 24–95.
- Sæmundsson, K., Axelsson, G., & Steingrímsson, B. (2009). Geothermal systems in global perspective. Short course on exploration for geothermal resources, UNU GTP, 11.
- Sæmundsson, K., Hjartarson, A., Kaldal, I., Sigurgeirsson, M. Ã., Kristinsson, S. G., & Víkingsson, S. (1999). Jarðfraeðikort af norðurgosbelti nyrðri hluti, 1:100.000. Reykjavík, Iceland GeoSurvey.
- Sæmundsson, K., Pringle, M., & Hardarson, B. (2000). About the age of strata in the Krafla volcanic system. In *Proceedings of the geoscience society of Iceland, spring meeting* (pp. 26–27).
- Sanyal, S. K., & Enedy, S. L. (2011). Fifty years of power generation at the geysers geothermal field, California–The lessons learned. In 36th workshop on geothermal reservoir engineering, Stanford, California.
- Schuler, J., Greenfield, T., White, R. S., Roecker, S. W., Brandsdóttir, B., Stock, J. M., et al. (2015). Seismic imaging of the shallow crust beneath the Krafla central volcano, NE Iceland. *Journal of Geophysical Research: Solid Earth*, 120(10), 7156–7173. https://doi.org/10.1002/ 2015jb012350
- Schuler, J., Pugh, D. J., Hauksson, E., White, R. S., Stock, J. M., & Brandsdóttir, B. (2016). Focal mechanisms and size distribution of earthquakes beneath the Krafla central volcano, ne Iceland. *Journal of Geophysical Research: Solid Earth*, 121(7), 5152–5168. https://doi.org/10.1002/2016/jbd13213
- Scott, S., O'Sullivan, J. P., Maclaren, O. J., Nicholson, R., Covell, C., Newson, J., & Guðjónsdóttír, M. S. (2022). Bayesian calibration of a natural state geothermal reservoir model, Krafla, north Iceland. *Water Resources Research*, 58(2), e2021WR031254. https://doi.org/10.1029/
- Sewell, S., Cumming, W., Bardsley, C., Winick, J., Quinao, J., Wallis, I., et al. (2015). Interpretation of microseismicity at the rotokawa geothermal field, 2008 to 2012. *Interpretation*, 19, 25.
- Tang, C., Rial, J. A., & Lees, J. M. (2008). Seismic imaging of the geothermal field at Krafla, Iceland using shear-wave splitting. *Journal of Volcanology and Geothermal Research*, 176(2), 315–324. https://doi.org/10.1016/j.jvolgeores.2008.04.017
- Thurber, C. H. (1992). Hypocenter-velocity structure coupling in local earthquake tomography. *Physics of the Earth and Planetary Interiors*, 75(1–3), 55–62. https://doi.org/10.1016/0031-9201(92)90117-e
- Vanorio, T., De Matteis, R., Zollo, A., Batini, F., Fiordelisi, A., & Ciulli, B. (2004). The deep structure of the Larderello-Travale geothermal field from 3D microearthquake traveltime tomography. *Geophysical Research Letters*, 31(7). https://doi.org/10.1029/2004gl019432
- Vanorio, T., Virieux, J., Capuano, P., & Russo, G. (2005). Three-dimensional seismic tomography from P wave and S wave microearthquake travel times and rock physics characterization of the Campi Flegrei Caldera. *Journal of Geophysical Research*, 110(B3). https://doi.org/10. 1029/2004ib003102
- Virieux, J., Amoroso, O., Gauthier, S., Got, J.-L., Jacques, J., Latorre, D., et al. (2015). Tomotv pl:first arrival delayed time tomography. GitHub [Software]. https://github.com/jeanvirieux/TOMOTV\_PL
- Virieux, J., Paul, A., Langlais, M., Janex, G., Gueguen, P., Helmstetter, A., & Stehly, L. (2024). Assessing the reliability of local earthquake tomography for crustal imaging: 30 yr of records in the western Alps as a case study. *Geophysical Journal International*, 236(1), 99–118. https://doi.org/10.1093/gji/ggad378
- Wassermann, J. (2012). Volcano seismology. In New manual of seismological observatory practice 2 (NMSOP-2) (pp. 1–77). Deutsches Geo-ForschungsZentrum GFZ.
- Watanabe, T. (1993). Effects of water and melt on seismic velocities and their application to characterization of seismic reflectors. Geophysical Research Letters, 20(24), 2933–2936. https://doi.org/10.1029/93gl03170
- Wessel, P., Smith, W. H., Scharroo, R., Luis, J., & Wobbe, F. (2013). Generic mapping tools: Improved version released [Software]. Eos, Transactions American Geophysical Union, 94(45), 409–410. https://doi.org/10.1002/2013eo450001

GLÜCK ET AL. 20 of 20